AGU PUBLICATIONS

Geophysical Research Letters

RESEARCH LETTER
10.1002/2017GL074513

First spaceborne phase altimetry over sea ice using TechDemoSat-1 GNSS-R signals

Weiqiang Li[1], Estel Cardellach[1], Fran Fabra[1], Antonio Rius[1], Serni Ribó[1], and Manuel Martín-Neira[2]

[1]Earth Observation Research Group, Institute of Space Sciences (CSIC-IEEC), Barcelona, Spain, [2]European Space Research and Technology Centre, European Space Agency, Noordwijk, Netherlands

Key Points:
- Spaceborne phase altimetry over sea ice using reflected Global Navigation Satellite System signal at 4.7 cm precision in 20 ms measurements
- Strong coherent component is found in sea ice reflected Global Positioning System signal received in space at high elevation angle
- Measured height residuals show good correlation with colocated sea ice thickness data from the Soil Moisture and Ocean Salinity mission

Supporting Information:
- Supporting Information S1

Correspondence to:
W. Li,
weiqiang@ice.csic.es

Citation:
Li, W., E. Cardellach, F. Fabra, A. Rius, S. Ribó, and M. Martín-Neira (2017), First spaceborne phase altimetry over sea ice using TechDemoSat-1 GNSS-R signals, *Geophys. Res. Lett.*, *44*, 8369–8376, doi:10.1002/2017GL074513.

Received 8 JUN 2017
Accepted 31 JUL 2017
Accepted article online 3 AUG 2017
Published online 17 AUG 2017

Abstract A track of sea ice reflected Global Navigation Satellite System (GNSS) signal collected by the TechDemoSat-1 mission is processed to perform phase altimetry over sea ice. High-precision carrier phase measurements are extracted from coherent GNSS reflections at a high angle of elevation (> 57°). The altimetric results show good consistency with a mean sea surface (MSS) model, and the root-mean-square difference is 4.7 cm with an along-track sampling distance of ~140 m and a spatial resolution of ~400 m. The difference observed between the altimetric results and the MSS shows good correlation with the colocated sea ice thickness data from Soil Moisture and Ocean Salinity. This is consistent with the reflecting surface aligned with the bottom of the ice-water interface, due to the penetration of the GNSS signal into the sea ice. Therefore, these high-precision altimetric results have potential to be used for determination of sea ice thickness.

1. Introduction

Global Navigation Satellite System reflectometry (GNSS-R) or PAsive Reflectometry and Interferometry System (PARIS) [*Martín-Neira*, 1993] can perform ocean altimetry along several tracks simultaneously. This passive wide-swath altimeter concept raises the possibility of resolving mesoscale features in ocean height. Significant impact of GNSS-R sea surface height (SSH) observations into mesoscale oceanographic models has been demonstrated by *Saynisch et al.* [2015] and *Li et al.* [2016] through simulation studies.

As in traditional radar altimeters (RA), GNSS-R measures the surface elevation through the time delay of the reflected signal. The time delay can be derived from the temporal evolution of the reflected radar pulse of GNSS ranging codes (referred to as code delay). GNSS-R code delay altimetry has been demonstrated in different experiments [e.g., *Lowe et al.*, 2002; *Rius et al.*, 2010; *Cardellach et al.*, 2014; *Mashburn et al.*, 2016; *Clarizia et al.*, 2016]. Dedicated spaceborne missions have been proposed [e.g., *Martín-Neira et al.*, 2011; *Wickert et al.*, 2016] to demonstrate such technique in low Earth orbiters.

GNSS carrier signals have short wavelength (~20 – 30 cm) compared to the chip length of their ranging codes (~30 – 300 m). As a consequence, the carrier phase information can be exploited to perform more precise altimetry over reflective surfaces. GNSS-R phase altimetry has been verified in different applications, such as ocean tides and sea ice observations from ground-based experiments [e.g., *Semmling et al.*, 2011; *Löfgren et al.*, 2011; *Fabra et al.*, 2012] and sea surface topography measurement from airborne platforms [e.g., *Semmling et al.*, 2014]. This technique is also planned to be demonstrated in the GNSS Reflectometry Radio Occultation and Scatterometry experiment aboard the International Space Station (GEROS-ISS). Initial simulations by *Semmling et al.* [2016] have shown that subdecimeter to meter level height precision can be achieved over sea surface depending on observation geometry and signal-to-noise ratio (SNR). However, carrier phase information can be only retrieved from coherent reflections of GNSS signal. For reflected GNSS signals received in space, coherent observations off the wind-driven sea are much less frequent due to diffuse reflection. The presence of sea ice at the water surface significantly shifts the diffuse reflection limit and improves the phase coherence of L band observations. Previous spaceborne data analysis results in [*Gleason*, 2006] have shown that GNSS signals reflected from sea ice exhibit strong coherent characteristics. In [*Cardellach et al.*, 2004], the carrier phase observations were retrieved from the GPS signals reflected from the Greenland ice sheet and Arctic sea ice with a spaceborne radio occultation setup. However, they were obtained at very low elevation angles (0° – 1°), which means reduced altimetric precision and potentially large tropospheric errors. So far, GNSS-R phase altimetry has never been demonstrated in space with enough altimetric precision at higher grazing angle (e.g., 5°–30° in elevation) or even near nadir (e.g., >45° in elevation).

This paper focuses on phase altimetry over sea ice using GNSS-R data collected by the Space GNSS Receiver Remote Sensing Instrument (SGR-ReSI) on board UK TechDemoSat-1 (TDS-1) [*Unwin et al.*, 2016]. The main data product, i.e., Level 1b data, is the Delay-Doppler Map (DDM) of GPS scattered power, which has been analyzed by different groups for various remote sensing applications, such as ocean scatterometry [e.g., *Foti et al.*, 2015], ocean altimetry [e.g., *Clarizia et al.*, 2016], and soil moisture [e.g., *Chew et al.*, 2016]. The DDMs collected over sea ice have been also analyzed for sea ice detection and sea ice concentration retrieval [e.g., *Yan and Huang*, 2016; *Yan et al.*, 2017; *Alonso-Arroyo et al.*, 2017]. With the DDM, only the coarse delay of the reflected signal can be extracted from the ranging code, resulting in a very low altimetry precision, e.g., 7.4–8.1 m precision over sea surface with 1 s observations [*Clarizia et al.*, 2016]. In addition to the DDM, the Level 0 (L0) raw samples have been also recorded occasionally, from which phase information of the reflected signal can be extracted. It offers an opportunity to examine high-precision phase altimetry over sea ice.

Sea ice altimetry has mainly been performed with laser altimeters (ICESat) and Ku band RA (e.g., Cryosat-2 and Envisat RA-2). Laser signals do not penetrate the sea ice (neither its snow cover), while Ku band microwaves penetrate the snow cover and in less extent the ice [*Laxon et al.*, 2013]. As reported in *Rivas et al.* [2010], *Cardellach et al.* [2012], and *Rius et al.* [2017], the penetration depths of the GPS signal into sea ice/ice sheet or dry-snow substructure can vary between tens of centimeters and 200–300 m. Considering the low L band dielectric contrast between the air and the sea ice (∼3) [*Fabra*, 2013, p26], it can be assumed that the signals reflected from the interface between the bottom of the ice and the sea water are the dominant components of the overall return echo, at least for certain sea ice characteristics (e.g., thickness, roughness, temperature, and salinity). In these cases, the altimetric measurement would be linked to the draft of the ice, offering a novel and complementary way to measure sea ice thickness. This study also aims to preliminarily assess this hypothesis. The rest of this paper is organized as follows: the data set and data processing chain are introduced in section 2, the altimeric retrieval and results are presented and discussed in section 3, and section 4 draws the conclusions.

2. Data Set and Data Processing

2.1. Description of the Data Set

Among other L0 raw collections publicly available at the MERRByS (Measurement of Earth Reflected Radio-navigation Signals By Satellite) website, the L0 raw collection in RD15 is the only one with sea ice reflected signals. This set of raw data was collected between 17:20:15.7 and 17:20:55.7 UTC on 18 January 2015, when TDS-1 passed over the northeast of Canada with the signal of GPS PRN-15 reflected from the Hudson Bay which was covered by concentrated sea ice, as shown in Figure 1. The elevation angle of PRN-15 at the specular point (SP) varied from 58.4° to 57.0°. Under this geometry, the size of the coherent reflection footprint, i.e., the first Fresnel zone, is estimated to be ∼ 400 m over the reflective surface [*Beckmann and Spizzichino*, 1987]. The same data set has been also processed and used for code delay altimetry in *Hu et al.* [2017], obtaining precisions of ∼1.0 m with 0.5 s observations.

The Special Sensor Microwave Imager and the Special Sensor Microwave Imager Sounder (SSM/I-SSMIS) sea ice concentration data published by the National Snow and Ice Data Center (NSIDC) [*Cavalieri et al.*, 2017] shows that the SP moved across the ice surface with 85%–100% total concentration. For reference, the sea ice thickness data derived from the Soil Moisture and Ocean Salinity (SMOS) mission [*Tian-Kunze et al.*, 2017] are also presented in Figure 1, which shows that the ice thickness was between 27 and 61 cm along the track of the SP.

The information about the receiver and transmitter position is not available in the accompanying metadata for this track. Two-line element sets (TLEs) of TDS-1 are obtained from the AGI satellite database server (https://support.agi.com/satdb/), and GPS precise orbit products have been collected from International GNSS Service (IGS) [*International GNSS Service*, 2017].

2.2. Data Processing

The processing of the raw samples consists of a closed-loop tracking of the direct signal and an open-loop tracking of the reflected signal, also known as the master-slave sampling [*Semmling et al.*, 2016] in GNSS-R phase altimetry. Through the raw samples processing, the power and phase of the reflected signal are

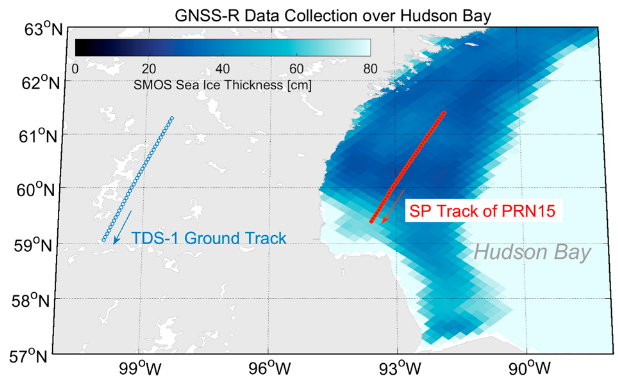

Figure 1. Ground tracks of TDS-1 and the specular point of GPS PRN-15 corresponding to the RD-15 raw collection between SoD (second of day (UTC)) 62,415.7 and 62,455.7 on 18 January 2015. The reflected signal was scattered from the sea ice over Hudson Bay. The sea ice thickness was obtained from the L3C SMOS Sea Ice Thickness data published by the Integrated Climate Data Center (ICDC).

extracted. To illustrate the characteristics of the sea ice reflected signal, one example of scattered power waveform is presented in Figure 2a together with a typical ocean reflected waveform for comparison. It can be observed that the waveform from the sea ice shows much higher peak power and much narrower waveform width, which means more specular characteristics due to small spreading of the scattered power over the reflective surface. These specular characteristics of the sea ice reflected signal were also justified by the traditional RA such as CryoSat-2 [*Kwok and Morison*, 2016]. It implies a significant coherent reflection component, which would make it possible to perform precise surface altimetry measurements.

According to *Semmling et al.* [2016], the SNR of the reflected waveform must be high enough (~30 dB) to mitigate unwrap errors. For this reason, a coherent integration time of 20 ms is used to estimate the residual phase of the reflected signal $\phi_r(t)$ after open-loop tracking. The residual phase is presented in Figure 2b, from which continuous phase observations can be seen except for the phase transitions within $\pm\pi$. This provides a clear evidence of the coherence of the signal reflected off the sea ice. The residual phase is then unwrapped to remove the phase transitions and yield continuous phase observations $\phi_r^{\mathrm{uwp}}(t)$ along the whole track.

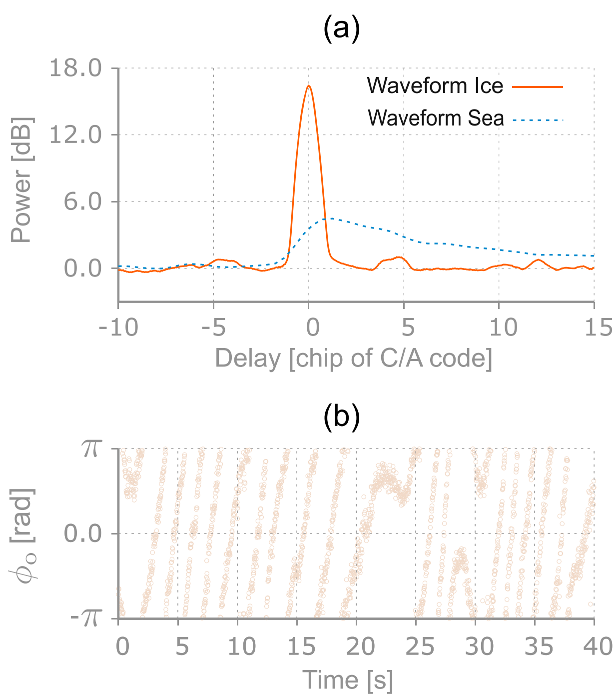

Figure 2. Characteristics of sea ice reflected signal for GPS PRN-15 in TDS-1 RD-15. (a) Comparison of the reflected power waveforms from sea surface and sea ice obtained with the TDS-1 satellite. Coherent integration time of 1 ms and incoherent average time of 1 s are used. Both waveforms have been normalized by the level of floor noise. (b) Residual phase of the reflected signal after open-loop tracking; the coherent integration time is 20 ms.

With the unwrapped phase residual of the reflected signal, the phase difference between the direct and the reflected signal can be computed by

$$\phi_o(t) = \int_0^t f_D^{\mathrm{dr}}(t_1)\mathrm{d}t_1 + \phi_r^{\mathrm{uwp}}(t) \quad (1)$$

in which f_D^{dr} is the open loop Doppler model used in master-slave sampling, the integral of f_D^{dr} yields the modeled phase difference between the direct and the reflected signals, and the integral interval corresponds to the period between the first signal sample and the epoch of measurement. The observed phase delay can be derived by $\rho_o^{\phi}(t) = \lambda_{L1}\phi_o(t)$ with λ_{L1} being the GPS L1 band carrier wavelength (~0.19 cm).

3. Altimetric Analysis

3.1. Phase Delay Model

In principle, the altimetric surface height can be linked to a residual geometric delay $\Delta\rho(t)$ between observation and model as

$$\begin{aligned}\Delta\rho(t) &= \rho_o(t) - \rho_m(t) \\ &= -2\sin e(t) \cdot h(t)\end{aligned} \quad (2)$$

in which $\rho_o(t)$ is the observed bistatic delay, $e(t)$ is the transmitter elevation angle seen from the SP, $h(t)$ is the altimetric surface height above a reference surface, and $\rho_m(t)$ is the modeled bistatic delay. It is worth mentioning that both the observed delay and the modeled delay include the geometric part and other systematic effects.

In reality, both the observation and model are contaminated by external and internal errors as well as delay mismodeling. The observed phase delay $\rho_o^\phi(t)$ can be expressed by

$$\begin{aligned}\rho_o^\phi(t) &= \rho_o(t) + \epsilon_o^\phi(t)\\ &= \rho_o(t) + b_o^{\text{int}} + \epsilon_o^{\text{n}}(t)\end{aligned} \tag{3}$$

in which $\epsilon_o^\phi(t)$ is the error in the phase delay observation, including an integer carrier cycle ambiguity b_o^{int} and a random noise term $\epsilon_o^{\text{n}}(t)$.

The modeled bistatic delay consists of the computation of the geometric delay followed by the application of a number of standard geophysical delay corrections:

$$\rho_m^\phi(t) = \rho_m^{\text{geom}}(t) + \rho_{\text{corr}}^{\text{ion}}(t) + \rho_{\text{corr}}^{\text{trop}}(t) + \rho_{\text{corr}}^{\text{tide}}(t) \tag{4}$$

in which the different terms on the right are explained next:

Geometric delay. The delay difference between the direct and reflected signal ρ_m^{geom} can be predicted from the transmitter, receiver, and estimated SP positions. Due to the lack of TDS-1 precise orbit information, the orbital position of the receiver was derived from the TLEs through Simplified General Perturbations Satellite Orbit Model 4 (SGP4). The transmitter position was interpolated from the IGS precise orbit. The position of the SP is predicted following Snell's law and taking the WGS84 ellipsoid as reference.

Geophysical delay corrections. The geophysical delay corrections applied to the bistatic delay include the ionospheric delay $\rho_{\text{corr}}^{\text{ion}}(t)$, the tropospheric delay $\rho_{\text{corr}}^{\text{trop}}(t)$, and the tidal correction $\rho_{\text{corr}}^{\text{tide}}(t)$. The ionospheric delay experienced by the reflected signal is estimated with the Tomographic Ionosphere model software [*Orús et al.*, 2005] from the Global Ionospheric Maps generated by UPC (see *Hernández-Pajares et al.* [2016] for a discussion on its performance in the context of IGS). The excess path delay due to the tropospheric effect is computed using the Hopfield model [*Hopfield*, 1971] with the meteorological parameters (temperature, pressure, and integrated water vapor) obtained from the reanalysis data of ECMWF (European Center for Medium range Weather Forecasting). The sea level elevation induced by ocean and solid Earth tides is derived and interpolated from the TPXO global ocean tide model [*Egbert and Erofeeva*, 2002] v7.2 and translated into the tidal correction. These geophysical delay correction terms are presented in Figures 3a–3c.

By considering the errors from the geometric delay and the geophysical delay corrections, the modeled bistatic delay can be expressed as

$$\rho_m^\phi(t) = \rho_m(t) + \epsilon_m^{\text{orb}}(t) + \epsilon_{\text{corr}}^{\text{res}}(t) \tag{5}$$

in which $\epsilon_m^{\text{orb}}(t)$ is the error induced by the orbit inaccuracy and $\epsilon_{\text{corr}}^{\text{res}}(t)$ is the residual of the geophysical delay corrections. With (3) and (5), the residual geometric delay can be expressed as

$$\begin{aligned}\Delta\rho^\phi(t) &= \rho_o^\phi(t) - \rho_m^\phi(t)\\ &= \Delta\rho(t) + \epsilon_{\Delta\rho}(t)\\ &= \Delta\rho(t) + \epsilon_o^\phi(t) - \epsilon_m^{\text{orb}}(t) - \epsilon_{\text{corr}}^{\text{res}}(t)\end{aligned} \tag{6}$$

in which different errors and corrections in both the modeled and observed delay appear explicitly.

The error due to the orbit uncertainty is the dominant one, as the accuracy of the receiver position predicted from TLEs/SGP4 is typically tens to hundreds of meters [*Levit and Marshall*, 2011] leading to a delay error with the same order of magnitude, which is far larger than the instrumental accuracy and the other correction residuals. Due to that, it is necessary to remove the orbit error term properly to investigate the altimetric surface height variability. For a very short orbit arc of observation (~2.5° in 40 s), the orbit error can be approximated by a linear trend. In fact, this kind of approximation has been well justified and was adopted in the data processing of early RA missions [e.g., in *Cheney et al.*, 1989].

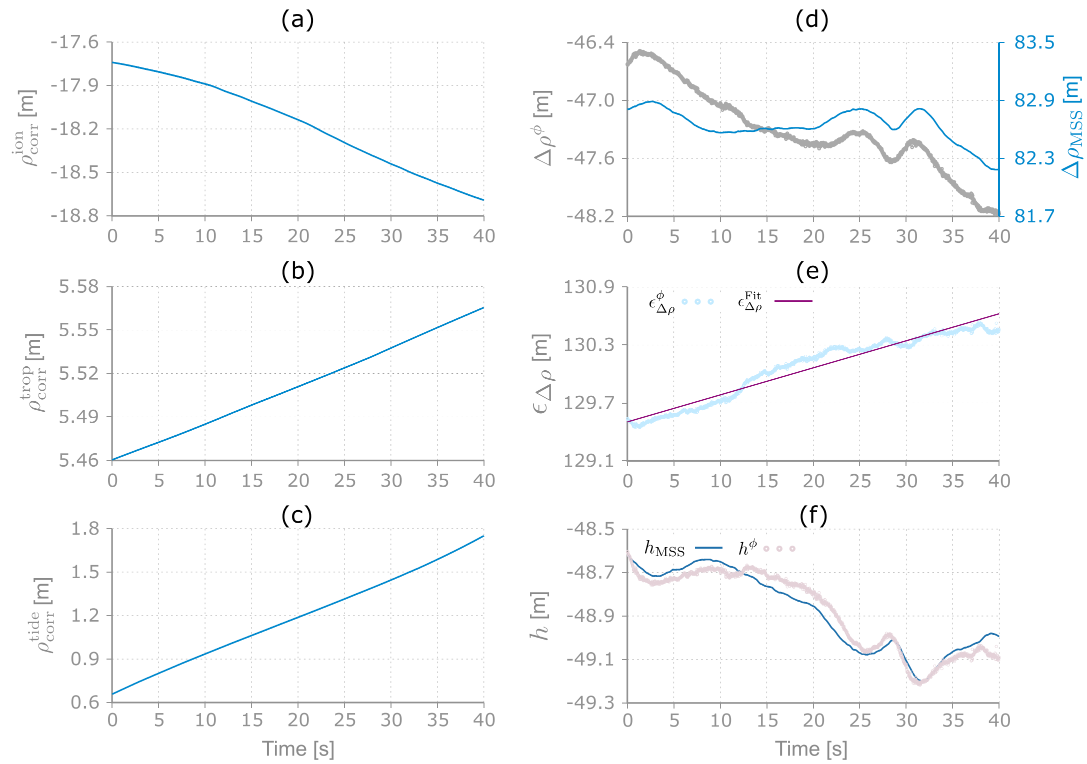

Figure 3. Altimetric retrieval from the phase delay observation of GPS PRN-15. (a) Ionospheric delay correction. (b) Tropospheric delay correction. (c) Tidal correction. (d) Comparison between the residual geometric delay $\Delta\rho^{\phi}(t)$ and that derived from the DTU13 MSS $\Delta\rho_{\rm MSS}(t)$. (e) Parametrization of the errors in the residual geometric delay by the linear function. (f) Comparison between the retrieved altimetric surface heights and the DTU13 MSS above the WGS84 ellipsoid.

3.2. Altimetric Retrieval and Results

To illustrate the aforementioned procedure, the measured residual geometric delay is computed from (6) and presented in Figure 3d together with a reference one. The latter is derived from the DTU13 mean sea surface (MSS) [*Andersen et al.*, 2014] by $\Delta\rho_{\rm MSS}(t) = -2h_{\rm MSS}(t)\sin e(t)$. It can be clearly seen that both delay curves have very similar fluctuation characteristics, which supports our data processing chain as well as demonstrates the sensitivity of phase delay observations to altimetric surface height variations.

However, there remains a significant difference in the trend between the two delay curves in Figure 3d which is mainly due to the orbit discrepancy according to (6). To proceed with the retrieval, this difference is formulated parametrically as a linear function of time, i.e.,

$$\epsilon_{\Delta\rho}^{\rm Fit}(t) = b_1 t + b_0 \tag{7}$$

with b_i ($i = 0, 1$) being the coefficients estimated with least squares fitting. For comparison, the parametrized error is presented in Figure 3e. It is worth mentioning that the linear components in other error terms, such as the integer carrier cycle ambiguity and the delay correction residuals, are also removed in addition to that in the orbit error term.

Once the error is parametrized, the altimetric surface height above the WGS84 ellipsoid $h^{\phi}(t)$ can be retrieved simply by

$$h^{\phi}(t) = -\frac{\Delta\rho^{\phi}(t) - \epsilon_{\Delta\rho}^{\rm Fit}(t)}{2\sin e(t)} \tag{8}$$

The retrieved altimetric surface heights are presented in Figure 3f together with the DTU13 mean SSH as the reference, from which it can be seen that the retrieved altimetric surface heights are in good consistency with the mean SSH. The root-mean-square difference (RMSD) between them, i.e., $\left\langle \left[h^{\phi}(t) - h_{\rm MSS}(t)\right]^2 \right\rangle^{1/2}$, is ~4.7 cm with an along-track sampling distance of ~140 m and a spatial resolution of ~400 m.

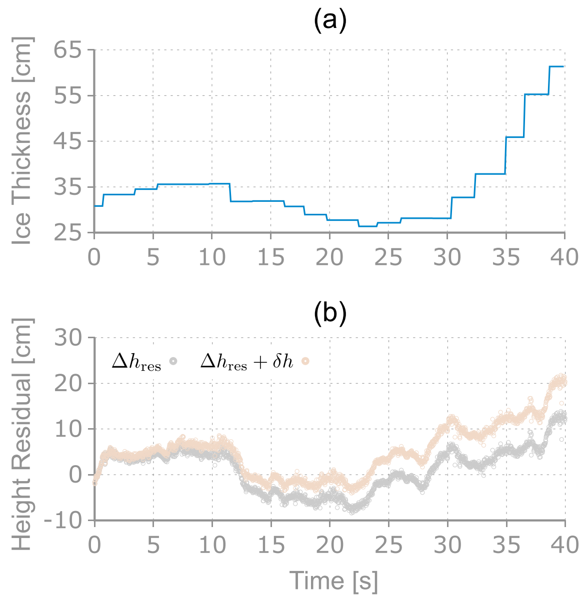

Figure 4. Comparison between the SMOS sea ice thickness profile and the height difference between the altimetric surface and the MSS. (a) SMOS sea ice thickness profile along the track of the SP. (b) Height difference between the altimetric surface and the MSS.

The presented altimetric results prove that the carrier phase observations of reflected GNSS signals are sensitive to the altimetric surface height variations. It should be remarked that the RMSDs between the altimetric surface height and the reference MSS do not fully represent the GNSS-R phase altimetry performance:

1. On the one hand, due to the linear approximation of the orbit error, the retrieved altimetric surface height is a relative measurement, which can only resolve the variation of surface height. However, this is a limitation of this particular experiment but not a general limitation of the technique.
2. On the other hand, the surface heights used as reference, i.e., the mean SSH, only represents the time-invariant component of the surface height, so that temporal changes in sea surface height could be another source of difference between the measured and the reference surface heights. Moreover, it is noted that the DTU13 MSS model in the Arctic Basin is derived from the long-term RA SSH observations coming from either open ocean or from water between ice floes [*Andersen et al.*, 2014] and thus is related neither to the sea ice thickness or its freeboard profile. A brief description on the relationship between the DTU13 MSS and the altimetric surface is provided in the supporting information.

3.3. Potential for Sea Ice Thickness Measurement

Analyzing the altimetric residuals, i.e., the difference between the retrieved elevation of the reflecting surface and the MSS, it is possible to assess the potential of GNSS-R altimetric observations for sea ice thickness measurement. As shown in Figure 1, the sea ice becomes thicker in the last segment (~10 s) of the data collection. In the same period, according to Figure 3f, the retrieved surface height is below the MSS, which indicates the existence of an excess delay due to signal penetration into the thicker sea ice. To quantitatively analyze this effect, the height difference between the altimetric surface and the MSS $\Delta h_{\mathrm{res}} = h_{\mathrm{MSS}} - h^{\phi}$ is computed and presented in Figure 4 together with the SMOS sea ice thickness profile along the SP track. It can be found that the evolution of the height difference is in good agreement with the transition of the sea ice thickness with the correlation coefficient between them being 0.71. Notice that the linear feature in Δh_{res} has been removed in the orbit error correction. By compensating a linear term $\delta h(t) = 0.2t$, the best correlation coefficient of 0.79 can be obtained.

According to Figure 4a, the ice thickness changed by ~34 cm along the reflection track. A significant fraction of the thickness (0.8 to 0.9) [*Wadhams et al.*, 1992; *Alexandrov et al.*, 2010] is under the flotation line, while only a small fraction represents the along-track variation of the freeboard profile (~4–7 cm). The total amplitude of the residual signal is ~25 cm, which is close to the height variation expected for the ice-water interface (~0.8 times the thickness variation). These findings also support the assumptions that the reflection's main contribution comes from the bottom of the sea ice.

4. Conclusion and Discussion

The sensitivity of spaceborne GNSS-R carrier phase observations to along-track variation of sea ice altimetric response has been presented by processing reflected GPS signals collected by the TechDemoSat-1 mission over sea ice. The smooth carrier phase observations are extracted by open-loop processing of the TDS-1 L0 raw samples. Due to the lack of orbit position of TDS-1, the receiver position is derived through the TLEs/SGP4 method, which induces a large orbit error in our delay measurements. These are limitations of the particular experiment analyzed in this study. This orbit error is approximated by a linear trend over the orbit arc and removed from the delay observations. Finally, the altimetric surface height is retrieved and compared against the DTU13 mean SSH. Preliminary results show that the RMSD between the measured surface height and the reference one is 4.7 cm with 20 ms phase delay observations (~140 m along-track sampling distance and ~400 m spatial resolution). This represents the first spaceborne GNSS-R carrier phase altimetric study at relatively high elevation angles (>57°).

GNSS signals are transmitted at L band, which penetrates snow and ice. Therefore, one of the relevant questions is the actual meaning of the "altimetric surface". From which layer does the "altimetric response" come from? This issue has preliminarily been studied by analyzing the altimetric residuals, i.e., the difference between the MSS and the altimetric solution. The variations of the residuals are proportional to the ice thickness (factor ⩾0.8), with lower altimetric height as the thickness increases (i.e., opposite sense than in laser and Ku band altimeters). These features are consistent with the draft variations associated to the thickness variations and therefore consistent with the hypothesis that the dominant reflecting layer is the interface between the bottom of the ice and sea water underneath. This finding, if confirmed in future experiments, would open the possibility to measure ice thickness from space in a way complementary to the current approaches. An advantage of measuring the draft is that its uncertainty propagates into thickness estimates with a smaller factor than the freeboard uncertainties. The data set analyzed corresponds to first year sea ice between 20 and 60 cm thickness, so the conclusions presented here should be revised for different sea ice conditions.

Further analyses and verifications of GNSS-R phase altimetry with different specular reflection conditions, e.g., over sea ice with different thickness and at different elevation angles (e.g., from near nadir to grazing angle) are left for future studies. Such research would rely on the availability of more extensive sets of raw data or complex waveforms acquisitions with TDS-1 and future spaceborne missions.

Acknowledgments
This work was supported in part by the Spanish Ministry of Economy and Competitiveness and EU/FEDER (ESP2015-70014-C2-2-R). The authors are grateful to Surrey Satellite Technology Ltd for making the TDS-1 Level 0 raw data publicly available through the MERRByS website (http://www.merrbys.org). The authors would like to thank ECMWF for providing the meteorological data. The authors are grateful to the National Snow and Ice Data Center for providing the SSM/I-SSMIS sea ice concentration data. The SMOS L3C sea ice thickness data published by the Integrated Climate Data Center (University of Hamburg, Germany) are appreciated. The authors also appreciate the help from Manuel Hernández-Pajares on computing the ionospheric delay of the reflected signal.

References

Alexandrov, V., S. Sandven, J. Wahlin, and O. M. Johannessen (2010), The relation between sea ice thickness and freeboard in the Arctic, *Cryosphere*, *4*(3), 373–380, doi:10.5194/tc-4-373-2010.

Alonso-Arroyo, A., V. U. Zavorotny, and A. Camps (2017), Sea ice detection using U.K. TDS-1 GNSS-R data, *IEEE Trans. Geosci. Remote Sens.*, *99*, 1–13, doi:10.1109/TGRS.2017.2699122.

Andersen, O., P. Knudsen, and L. Stenseng (2014), The DTU13 MSS (Mean Sea Surface) and MDT (Mean Dynamic Topography) from 20 years of satellite altimetry, in *IGFS 2014: Proceedings of the 3rd International Gravity Field Service (IGFS), Shanghai, China, 30 Jun.–6 Jul.*, edited by S. Jin and R. Barzaghi, pp. 111–121, Springer Int. Publ., Cham, Switzerland, doi:10.1007/1345_2015_182.

Beckmann, P., and A. Spizzichino (1987), *The Scattering of Electromagnetic Waves From Rough Surfaces*, Artech House, Norwood, Mass.

Cardellach, E., C. Ao, M. De la Torre Juárez, and G. Hajj (2004), Carrier phase delay altimetry with GPS-reflection/occultation interferometry from low Earth orbiters, *Geophys. Res. Lett.*, *31*, L10402, doi:10.1029/2004GL019775.

Cardellach, E., F. Fabra, A. Rius, S. Pettinato, and S. D'Addio (2012), Characterization of dry-snow sub-structure using GNSS reflected signals, *Remote Sens. Environ.*, *124*, 122–134, doi:10.1016/j.rse.2012.05.012.

Cardellach, E., A. Rius, M. Martín-Neira, F. Fabra, O. Nogués-Correig, S. Ribó, J. Kainulainen, A. Camps, and S. D'Addio (2014), Consolidating the precision of interferometric GNSS-R ocean altimetry using airborne experimental data, *IEEE Trans. Geosci. Remote Sens.*, *52*(8), 4992–5004, doi:10.1109/TGRS.2013.2286257.

Cavalieri, D., C. Parkinson, P. Gloersen, and H. Zwally (2017), Sea ice concentrations from Nimbus-7 SMMR and DMSP SSM/I-SSMIS passive microwave data, Version 1. NASA DAAC at the National Snow and Ice Data Center, Boulder, Colo. [Available at http://nsidc.org/data/NSIDC-0051/versions/1.]

Cheney, R. E., B. C. Douglas, and L. Miller (1989), Evaluation of Geosat altimeter data with application to tropical Pacific sea level variability, *J. Geophys. Res.*, *94*(C4), 4737–4747, doi:10.1029/JC094iC04p04737.

Chew, C., R. Shah, C. Zuffada, G. Hajj, D. Masters, and A. J. Mannucci (2016), Demonstrating soil moisture remote sensing with observations from the UK TechDemoSat-1 satellite mission, *Geophys. Res. Lett.*, *43*, 3317–3324, doi:10.1002/2016GL068189.

Clarizia, M. P., C. Ruf, P. Cipollini, and C. Zuffada (2016), First spaceborne observation of sea surface height using GPS-Reflectometry, *Geophys. Res. Lett.*, *43*, 767–774, doi:10.1002/2015GL066624.

Egbert, G. D., and S. Y. Erofeeva (2002), Efficient inverse modeling of barotropic ocean tides, *J. Atmos. Oceanic Technol.*, *19*(2), 183–204, doi:10.1175/1520-0426(2002)019<0183:EIMOBO>2.0.CO;2.

Fabra, F. (2013), GNSS-R as a source of opportunity for remote sensing of the cryosphere, PhD thesis, Universitat Politècnica de Catalunya, Barcelona, Spain.

Fabra, F., E. Cardellach, A. Rius, S. Ribo, S. Oliveras, O. Nogues-Correig, M. B. Rivas, M. Semmling, and S. D'Addio (2012), Phase altimetry with dual polarization GNSS-R over sea ice, *IEEE Trans. Geosci. Remote Sens.*, *50*(6), 2112–2121, doi:10.1109/TGRS.2011.2172797.

Foti, G., C. Gommenginger, P. Jales, M. Unwin, A. Shaw, C. Robertson, and J. Roselló (2015), Spaceborne GNSS reflectometry for ocean winds: First results from the UK TechDemoSat-1 mission, *Geophys. Res. Lett.*, *42*, 5435–5441, doi:10.1002/2015GL064204.

Gleason, S. (2006), Remote sensing of ocean, ice and land surfaces using bistatically scattered GNSS signals from low Earth orbit, PhD thesis, Univ. of Surrey, Guildford, U. K.

Hernández-Pajares, M., D. Roma Dollase, A. Krankowski, A. García Rigo, and R. Orús Pérez (2016), Comparing performances of seven different global VTEC ionospheric models in the IGS context, paper presented at International GNSS Service Workshop (IGS 2016), International GNSS Service (IGS), Sydney, Australia, 8-12 Feb.

Hopfield, H. S. (1971), Tropospheric effect on electromagnetically measured range: Prediction from surface weather data, *Radio Sci.*, *6*(3), 357–367, doi:10.1029/RS006i003p00357.

Hu, C., C. Benson, C. Rizos, and L. Qiao (2017), Single-pass sub-meter space-based GNSS-R ice altimetry: Results from TDS-1, *IEEE J. Sel. Top. Appl. Earth Obs. Remote Sens.*, *7*(99), 1493–1500, doi:10.1109/JSTARS.2014.2320298.

International GNSS Service (2017), *GNSS Final Combined Orbit Solution Product*,NASA Crustal Dynamics Data Information System (CDDIS), Greenbelt, Md., doi:10.5067/gnss/gnss_igsorb_001.

Kwok, R., and J. Morison (2016), Sea surface height and dynamic topography of the ice-covered oceans from CryoSat-2: 2011–2014, *J. Geophys. Res. Oceans*, *121*, 674–692, doi:10.1002/2015JC011357.

Laxon, S. W., et al. (2013), CryoSat-2 estimates of Arctic sea ice thickness and volume, *Geophys. Res. Lett.*, *40*, 732–737, doi:10.1002/grl.50193.

Levit, C., and W. Marshall (2011), Improved orbit predictions using two-line elements, *Adv. Space Res.*, *47*(7), 1107–1115, doi:10.1016/j.asr.2010.10.017.

Li, Z., C. Zuffada, S. T. Lowe, T. Lee, and V. Zlotnicki (2016), Analysis of GNSS-R altimetry for mapping ocean mesoscale sea surface heights using high-resolution model simulations, *IEEE J. Sel. Top. Appl. Earth Obs. Remote Sens.*, *9*(10), 4631–4642, doi:10.1109/JSTARS.2016.2581699.

Löfgren, J., R. Haas, H.-G. Scherneck, and M. Bos (2011), Three months of local sea level derived from reflected GNSS signals, *Radio Sci.*, *46*, RS0C05, doi:10.1029/2011RS004693.

Lowe, S. T., C. Zuffada, Y. Chao, P. Kroger, L. E. Young, and J. L. LaBrecque (2002), 5-cm-precision aircraft ocean altimetry using GPS reflections, *Geophys. Res. Lett.*, *29*(10), 1375, doi:10.1029/2002GL014759.

Martín-Neira, M. (1993), A passive reflectometry and interferometry system (PARIS): Application to ocean altimetry, *ESA J.*, *17*(4), 331–355.

Martín-Neira, M., S. D'Addio, C. Buck, N. Floury, and R. Prieto-Cerdeira (2011), The PARIS ocean altimeter in-orbit demonstrator, *IEEE Trans. Geosci. Remote Sens.*, *49*(6), 2209–2237, doi:10.1109/TGRS.2010.2092431.

Mashburn, J., P. Axelrad, S. T. Lowe, and K. M. Larson (2016), An assessment of the precision and accuracy of altimetry retrievals for a Monterey Bay GNSS-R experiment, *IEEE J. Sel. Top. Appl. Earth Obs. Remote Sens.*, *9*(10), 4660–4668, doi:10.1109/JSTARS.2016.2537698.

Orús, R., M. Hernández-Pajares, J. Juan, and J. Sanz (2005), Improvement of global ionospheric VTEC maps by using kriging interpolation technique, *J. Atmos. Sol. Terr. Phys.*, *67*(16), 1598–1609, doi:10.1016/j.jastp.2005.07.017.

Rius, A., E. Cardellach, and M. Martin-Neira (2010), Altimetric analysis of the sea-surface GPS-reflected signals, *IEEE Trans. Geosci. Remote Sens.*, *48*(4), 2119–2127, doi:10.1109/TGRS.2009.2036721.

Rius, A., E. Cardellach, F. Fabra, W. Li, S. Ribó, and M. Hernández-Pajares (2017), Feasibility of GNSS-R ice sheet altimetry in Greenland using TDS-1, *Remote Sens.*, *9*(7), 742, doi:10.3390/rs9070742.

Rivas, M. B., J. A. Maslanik, and P. Axelrad (2010), Bistatic scattering of GPS signals off Arctic sea ice, *IEEE Trans. Geosci. Remote Sens.*, *48*(3), 1548–1553, doi:10.1109/TGRS.2009.2029342.

Saynisch, J., M. Semmling, J. Wickert, and M. Thomas (2015), Potential of space-borne GNSS reflectometry to constrain simulations of the ocean circulation, *Ocean Dyn.*, *65*(11), 1441–1460, doi:10.1007/s10236-015-0886-y.

Semmling, A. M., et al. (2011), Detection of Arctic Ocean tides using interferometric GNSS-R signals, *Geophys. Res. Lett.*, *38*, L04103, doi:10.1029/2010GL046005.

Semmling, A., J. Beckheinrich, J. Wickert, G. Beyerle, S. Schön, F. Fabra, H. Pflug, K. He, J. Schwabe, and M. Scheinert (2014), Sea surface topography retrieved from GNSS reflectometry phase data of the GEOHALO flight mission, *Geophys. Res. Lett.*, *41*, 954–960, doi:10.1002/2013GL058725.

Semmling, A. M., V. Leister, J. Saynisch, F. Zus, S. Heise, and J. Wickert (2016), A phase-altimetric simulator: Studying the sensitivity of Earth-reflected GNSS signals to ocean topography, *IEEE Trans. Geosci. Remote Sens.*, *54*(11), 6791–6802, doi:10.1109/TGRS.2016.2591065.

Tian-Kunze, X., L. Kaleschke, and N. Maaß (2017), SMOS daily sea ice thickness version 3. Integrated Climate Data Center (ICDC), Univ. of Hamburg, Hamburg, Germany. [Available at http://icdc.cen.uni-hamburg.de/.]

Unwin, M., P. Jales, J. Tye, C. Gommenginger, G. Foti, and J. Rosello (2016), Spaceborne GNSS-reflectometry on TechDemoSat-1: Early mission operations and exploitation, *IEEE J. Sel. Top. Appl. Earth Obs. Remote Sens.*, *9*(10), 4525–4539, doi:10.1109/JSTARS.2016.2603846.

Wadhams, P., W. B. Tucker, W. B. Krabill, R. N. Swift, J. C. Comiso, and N. R. Davis (1992), Relationship between sea ice freeboard and draft in the Arctic Basin, and implications for ice thickness monitoring, *J. Geophys. Res.*, *97*(C12), 20,325–20,334, doi:10.1029/92JC02014.

Wickert, J., et al. (2016), GEROS-ISS: GNSS reflectometry, radio occultation, and scatterometry onboard the International Space Station, *IEEE J. Sel. Top. Appl. Earth Obs. Remote Sens.*, *9*(10), 4552–4581, doi:10.1109/JSTARS.2016.2614428.

Yan, Q., and W. Huang (2016), Spaceborne GNSS-R sea ice detection using delay-doppler maps: First results from the U.K. TechDemoSat-1 mission, *IEEE J. Sel. Top. Appl. Earth Obs. Remote Sens.*, *9*(10), 4795–4801, doi:10.1109/JSTARS.2016.2582690.

Yan, Q., W. Huang, and C. Moloney (2017), Neural networks based sea ice detection and concentration retrieval from GNSS-R Delay-Doppler Maps, *IEEE J. Sel. Top. Appl. Earth Obs. Remote Sens.*, *PP*(99), 1–10, doi:10.1109/JSTARS.2017.2689009.